

Numerical simulations of parasitic folding in multilayers

Marcel Frehner, Stefan M. Schmalholz*

Department of Earth Sciences, Geological Institute, ETH Zurich, 8092 Zurich, Switzerland

Received 6 December 2005; received in revised form 19 May 2006; accepted 22 May 2006

Available online 25 July 2006

Abstract

We use the finite element method to simulate slow viscous (Newtonian) flow in two dimensions without gravity and to model asymmetric (S- and Z-shaped) and symmetric (M-shaped) parasitic folds during multilayer folding. During multilayer folding, the matrix between stiffer layers shows a deformation close to pure shear in the hinge area and a combination of pure and simple shear in the limb areas. Thinner layers placed between thicker layers develop symmetric parasitic folds in the hinge, and eventually asymmetric parasitic folds in the limbs of the larger fold. Our results verify numerically the theory that asymmetric parasitic folds develop from symmetric buckle-folds that are sheared by the hingeward relative displacement of the thick layers in the limbs of the first-order fold. To develop asymmetric shapes, the amplitudes of the parasitic folds must exceed a critical value before the first-order fold begins to amplify. Otherwise, the parasitic folds are unfolded during flattening that takes place in the limb area between the thick layers. More than five thin layers are necessary to generate distinct asymmetric parasitic folds for the applied model setting. More layers generate higher amplification rates in the thin layers and, hence, higher amplitudes.

© 2006 Elsevier Ltd. All rights reserved.

Keywords: Parasitic folds; Multilayers; Folding; Buckling; Finite element method

1. Introduction

Parasitic folds are common in folded multilayer sequences (Fig. 1). Parasitic folds are “folds of small wavelengths and amplitudes located within folds of larger wavelengths and amplitudes in situations of polyharmonic folding. Parasitic folds normally show S- or Z-shaped asymmetric forms in the limbs of the larger structure (sometimes termed drag folds) and symmetric M forms in hinge zones” (Ramsay and Huber, 1987). The term “parasitic fold” was established by DeSitter (1964) and replaced the older term “drag fold”. Drag folds were often considered to result from layer-parallel shearing of incompetent layers (e.g., Williams, 1961), whereas a buckling instability was not considered to be essential. In contrast to the shearing theory, Ramberg (1963, 1964) applied the dominant wavelength concept of Biot (1961) and showed

theoretically and experimentally that parasitic folds (Ramberg still used the term drag fold) may form in multilayer sequences, if the individual layers have different thicknesses and mechanical strengths (i.e. viscosity, if the layers are Newtonian fluids). Ramberg (1963) showed that parasitic folds develop in two stages: first, a buckling instability generates symmetric folds and, second, the symmetric buckles are sheared and become asymmetric. Shearing is caused by folding of thicker layers, which exhibit much larger wavelengths than the parasitic folds in the thin layers between the thick layers.

Although there are many theoretical (e.g., Biot, 1965; Johnson, 1969; Johnson and Fletcher, 1994), analogue (e.g., Cobbold et al., 1971; Ghosh, 1968; Ramberg and Strömgaard, 1971) and numerical (e.g., Casey and Huggenberger, 1985; Debrenmaecker and Becker, 1978; Schmalholz et al., 2001) studies of multilayer folding, few of these studies were concerned with the formation of parasitic folds (e.g., Pfaff and Johnson, 1989; Ramberg, 1963). In this study, we perform numerical simulations of multilayer folding in two dimensions to test and quantify the theory of parasitic folding for Newtonian

* Corresponding author. Tel.: +41 44 632 81 67; fax: +41 44 632 10 30.

E-mail addresses: frehner@erdw.ethz.ch (M. Frehner), schmalholz@erdw.ethz.ch (S.M. Schmalholz).



Fig. 1. Asymmetric, S- and Z-shaped, parasitic folds in folded, foliated metagabbros, Val Malenco, Southern Swiss Alps (picture courtesy of Jean-Pierre Burg).

viscous materials. Ramberg (1963) verified his theory with analogue experiments using elastic materials. We performed numerical simulations because they provide more information than analogue experiments. Advantages of the numerical approach are: (i) the rheological properties can be defined exactly, whereas for analogue materials the exact rheology is often difficult to quantify, (ii) all boundary conditions are known, (iii) the contact between individual layers can be welded, whereas some amount of interlayer gliding cannot be excluded in analogue experiments, and (iv) the strains, strain rates and stresses are calculated at any point within the numerical model domain.

The particular aim of this study is to model parasitic folding in multilayers having at least one order of magnitude larger wavelengths than the parasitic folds. A particular goal is to generate distinct asymmetric parasitic fold forms in the limbs of the larger fold. This is not trivial for a pure shear background deformation with a shortening direction parallel to the initially flat layers (Ramberg, 1963). Therefore, the strain evolution is thoroughly investigated using finite strain ellipses calculated from the numerically computed velocity field. Several studies (e.g., Mühlhaus et al., 2002; Ramberg, 1961; Schmid and Podlachikov, 2006) showed that the number of layers in multilayer systems and the resulting anisotropy have a strong effect on the amplification rates of the individual

layers. Therefore, we vary the number of thin layers in our experiments and show that a minimum number of thin layers (approx. >5) is required to generate parasitic folds with distinct asymmetric shapes.

We first describe the model setting and the numerical algorithm, which is based on the finite element method (see Appendix), and how we calculate the finite strain ellipse from the numerical results. Then, we consider folding of two, equally thick, viscous layers embedded in less viscous material. We quantify the strain distribution and evolution in the area between the two layers. Next, thinner layers having the same viscosity as the thick layers are placed between the two thick layers. We investigate the impact of the initial amplitude and of the number of thin layers on the parasitic fold development.

2. Methods

2.1. Model setting

The governing continuum mechanics equations describing slow, viscous, incompressible flow in two dimensions are solved with the finite element method (e.g., Cuvelier et al., 1986; Hughes, 1987; Thomasset, 1981). The numerical simulations have been performed with the self-developed algorithm presented in the Appendix. All physical properties are non-dimensionalized using three characteristic values given in Table 1. Both the mechanically strong layers and the embedding material have a Newtonian rheology and the viscosity contrast is 100 which leads to an active amplification of all the stiff layers. Boundary conditions are free slip at the lower and left boundary, free surface at the upper boundary and free slip with prescribed horizontal velocity at the right boundary. The horizontal velocity is modified at every time step to enforce a constant background shortening strain rate. Differences in fold wavelengths are controlled by differences in initial layer thicknesses and differences in fold amplification are controlled by differences in initial amplitudes. Initial conditions and other parameters are given in Table 2. The velocities are only specified at the boundaries of the model domain so that during shortening a true wavelength selection takes place for all layers.

2.2. Finite strain ellipse

The finite strain ellipse is a geometrical tool to display the strain field (e.g., Ramsay and Huber, 1983) and is here calculated from the numerically computed velocity field. For every numerical time step the components of the velocity gradient

Table 1
Characteristic values used for non-dimensionalization of all other physical quantities

Char. length scale	(Thickness of thick layer)/5
Char. time scale	1/(Shortening strain rate)
Char. viscosity	Viscosity of matrix

Table 2
Model parameters for both two-layer and multilayer simulations

Setup for numerical experiments (dimensionless parameters)	
Viscosity layers	$\mu_{\text{stiff}} = 100$
Viscosity embedding material	$\mu_{\text{matrix}} = 1$
Initial thickness	
Thick layers	$H_{\text{thick } 0} = 5$
Thin layers (multilayers only)	$H_{\text{thin } 0} = 0.1$
Material above and below thick layers	$H_{\text{matrix outer}} = 20$
Material between layers (multilayers only)	$H_{\text{matrix } 0} = 0.3$
Width of domain	$L_0 = 40$
Initial perturbation	
Thick layers	Half cosine wave.
Thin layer (multilayers only)	Random white noise.
	$A_{\text{thin } 0}/H_{\text{thin } 0} = 0.1$
Time step	$\Delta t = 5 \times 10^{-3}$

All values have been non-dimensionalized with the characteristic scales presented in Table 1.

tensor are calculated at each point within the numerical domain. The velocity gradient tensor is used to calculate the new coordinates (x', y') of an arbitrary point P after a deformation increment, if the initial coordinates (x, y) are known. The tensor relating the incremental deformation is here called incremental deformation gradient tensor $\mathbf{G}^{(t)}$ and defined by the relation

$$\begin{Bmatrix} x' \\ y' \end{Bmatrix}_P = \underbrace{\begin{bmatrix} 1 + \Delta t \frac{\partial v_x}{\partial x} & \Delta t \frac{\partial v_x}{\partial y} \\ \Delta t \frac{\partial v_y}{\partial x} & 1 + \Delta t \frac{\partial v_y}{\partial y} \end{bmatrix}}_{\mathbf{G}^{(t)}} \begin{Bmatrix} x \\ y \end{Bmatrix}_P \quad (1)$$

where v_x and v_y are velocities in the x - and the y -direction, respectively, Δt is the time interval between two consecutive deformation increments and the superscript symbol t refers to the time step. After a second deformation increment, direct

substitution of Eq. (1) yields the new coordinates (x'', y'') of point P as

$$\begin{Bmatrix} x'' \\ y'' \end{Bmatrix}_P = \mathbf{G}^{(2)} \begin{Bmatrix} x' \\ y' \end{Bmatrix}_P = \mathbf{G}^{(2)} \mathbf{G}^{(1)} \begin{Bmatrix} x \\ y \end{Bmatrix}_P \quad (2)$$

According to this multiplicative coordinate transformation, the coordinates of point P can be calculated for any number of deformation increments. Multiplication of all incremental deformation gradient tensors leads to the finite deformation gradient tensor \mathbf{F} that directly connects the final coordinates with the initial coordinates. Point P may be initially an arbitrary point on a circle centred on an integration point of a finite element. Assuming homogeneous deformation around this integration point during all deformation steps, the coordinates of the deformed circle can also be calculated (Fig. 2). Our formulation to calculate the finite strain ellipse is in accordance with Ramsay and Huber (1983, Appendix B). The principal strain axes correspond to the eigenvalues of the tensor $\mathbf{F}^T \mathbf{F}$ (superscript symbol T represents the transpose of the tensor) which is the right Cauchy–Green tensor (Haupt, 2002).

The finite deformation gradient tensor is calculated for specific points within the numerical domain and is updated at every time step. It can be averaged over an area or interpolated to every point, like every other quantity. Therefore, finite strain ellipses can be drawn everywhere and at every size within the numerical domain. However, a strain ellipse represents only the strain at a certain point assuming that the area covered by the finite strain ellipse has undergone homogeneous strain.

In natural deformation it is possible that at a certain location compression follows extension or vice versa. This means that a circle can be changed into an ellipse, which afterwards is deformed back to a circle. The resulting finite strain circle does not readily express total strain. The same strain resetting is true for rigid body rotations. To remove this shortcoming and to be able to distinguish between truly undeformed circles and deformed, but circular finite strain ellipses, we assign colours to the calculated finite strain ellipses according to the

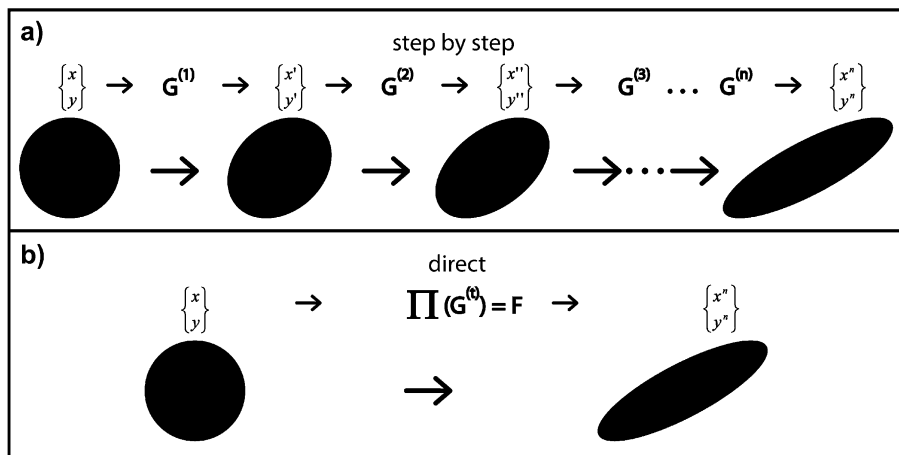


Fig. 2. (a) Progressive deformation of a strain ellipse during simple shear. To calculate the new coordinates of the ellipse after each deformation increment, Eq. (1) is applied to the coordinates of the ellipse. (b) Direct calculation of the coordinates of the finite strain ellipse using Eq. (2). The finite deformation gradient tensor \mathbf{F} has to be calculated beforehand.

accumulated von Mises equivalent strain and the finite rotation angle due to rigid body rotation. The accumulated von Mises equivalent strain, $\varepsilon_{\text{eqv}}^{\text{accumulated}}$, and the rotation angle, α , are

$$\varepsilon_{\text{eqv}}^{\text{accumulated}} = \sum_{\text{timesteps}} \varepsilon_{\text{eqv}}^{\text{incremental}} = \sum_{\text{timesteps}} \sqrt{\frac{2}{3}(\varepsilon_{xx}^2 + \varepsilon_{yy}^2 + 2\varepsilon_{xy}^2)} \quad (3)$$

$$\alpha = \sum_{\text{timesteps}} \arctan(\omega_{yx}) \quad (4)$$

where ε_{xx} , ε_{yy} and ε_{xy} are the components of the incremental strain tensor and ω_{yx} is the incremental spin (positive counterclockwise):

$$\varepsilon_{xx} = \Delta t \frac{\partial v_x}{\partial x}, \quad \varepsilon_{yy} = \Delta t \frac{\partial v_y}{\partial y}, \quad \varepsilon_{xy} = \frac{\Delta t}{2} \left(\frac{\partial v_x}{\partial y} + \frac{\partial v_y}{\partial x} \right),$$

$$\omega_{yx} = \frac{\Delta t}{2} \left(\frac{\partial v_y}{\partial x} - \frac{\partial v_x}{\partial y} \right) \quad (5)$$

The von Mises equivalent strain is a measure of the total change of shape and is always positive. Both quantities are scalar and can be summed up over all deformation steps, leading to a value for the shape change history and the finite rotation angle, respectively. While the shape of the strain ellipses represents the final deformation stage, the colours provide information about the deformation history (Fig. 3).

3. Finite strain in two-layer folds

Simulations of multilayer folding include two thick layers above and below thinner layers. The strain distribution and evolution during folding of two thick layers with a homogeneous matrix in between is first investigated. Both layers initially exhibit a sinusoidal perturbation corresponding to the theoretical dominant wavelength for single-layer folding (Fletcher, 1977); the initial ratio of amplitude to layer thickness is 0.01. Finite strain ellipses are coloured with the accumulated von Mises equivalent strain and the finite rotation angle for 40% horizontal bulk shortening (Fig. 3). Compared to the matrix, the layers show little strain and the dominant deformation in these layers involves rigid body rotation. Rotation and deformation are strong in the matrix (red colours on the left- and right-hand side) and rotation is in opposite direction to the rotation in the layers. The simultaneous rotations and shape changes indicate that the main part of the deformation is layer-parallel shearing. The thickness of the matrix measured orthogonal to the layer interfaces changes from hinge to inflexion point. It becomes thicker in the hinge zone and thinner in the limbs. At the same time, the two layers tend to form parallel folds (the orthogonal layer thickness is constant over the whole wavelength).

The matrix can be divided into three regions that undergo different deformation paths: (i) near the inflexion point the matrix is characterized by layer-parallel shortening, followed by layer-parallel shearing and layer-normal flattening, (ii) near the hinge zone the matrix deformation is characterized by

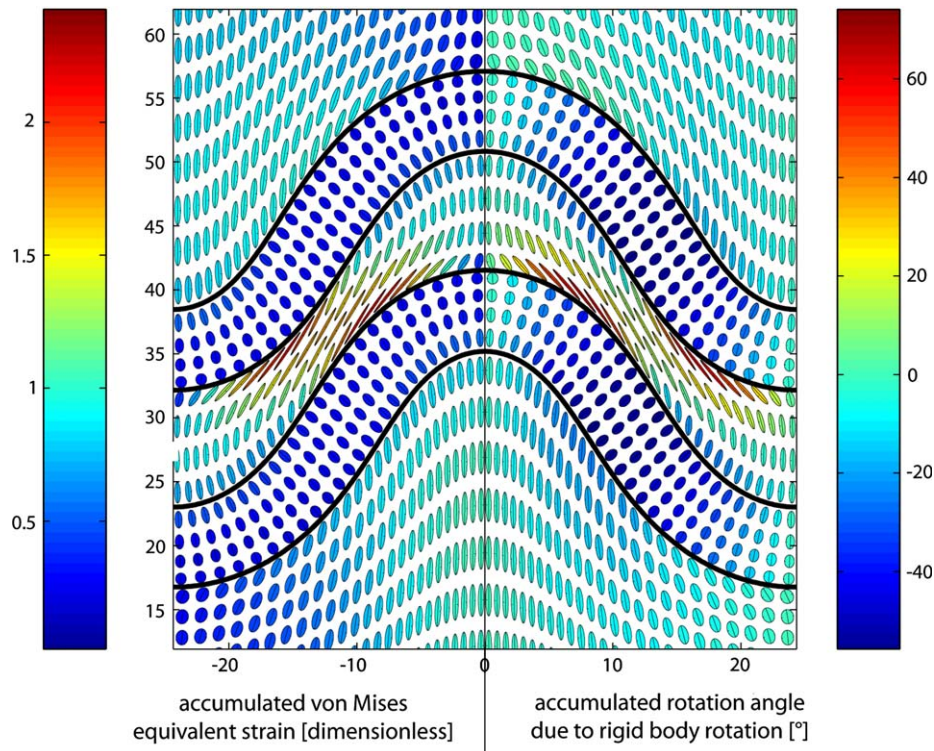


Fig. 3. Two folded viscous layers after 40% bulk shortening. Viscosity contrast between layers and embedding material is 100. The initial distance between the two layers is equal to the layer thickness. Strain ellipses on the left-hand side are coloured with accumulated von Mises equivalent strain, ellipses on the right-hand side are coloured with finite rigid body rotation angle.

layer-parallel shortening during the whole folding history so that total strain can be approximated by pure shear, and (iii) a transition zone between regions (i) and (ii), where the two different deformation regions interfere. In Fig. 4, nine originally vertical beams deformed with the numerically calculated velocity field are plotted together with the corresponding finite strain ellipses. Each beam initially consisted of five squares. After 10% bulk shortening (Fig. 4a) the matrix is shortened horizontally without any simple shear deformation. After 25% bulk shortening (Fig. 4b) simple shear is stronger near the convex interface and strongest between the inflexion point and the hinge. This is marked in the middle beam in the matrix which deforms asymmetrically with a very strong strain near the convex interface and a weaker strain near the concave interface. The beam at the inflexion point of the matrix,

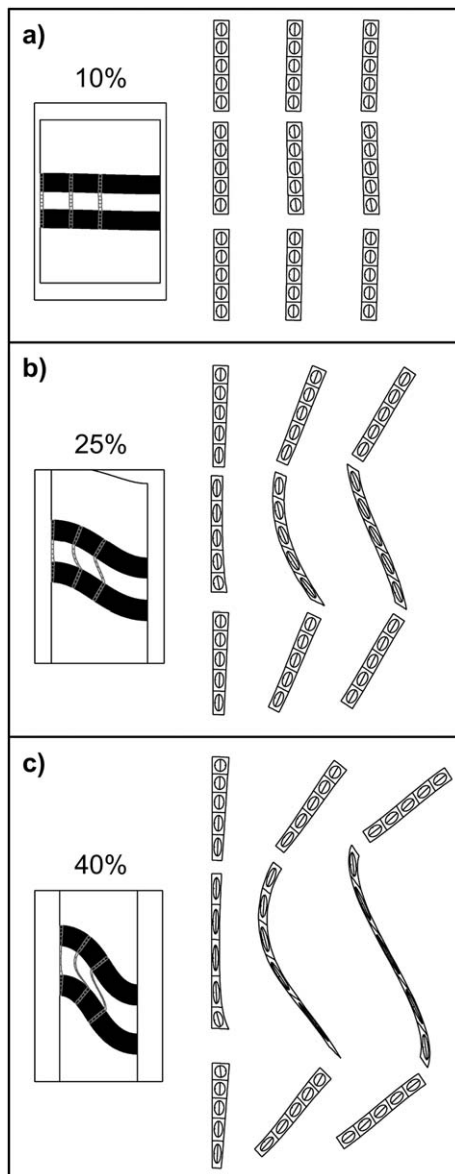


Fig. 4. Finite strain evolution for the two folded layers shown in Fig. 3. Nine beams, three in each stiffer layer and three in the material between the layers, initially consisted of five squares each. The location of the beams is shown in the half fold (left-hand side).

however, deforms symmetrically. After 40% bulk shortening (Fig. 4c) the middle beam in the matrix develops a strongly strained tail at the convex interface. This tail extends between the two layers into the zone influenced by flattening normal to the layer interfaces. Flattening starts when the limbs of the two layers move towards each other during fold amplification. Therefore, the tail of the middle beam in the matrix results from simple shearing and flattening; flattening intensifies the strongly elongated shape of the finite strain ellipses. The same shearing–flattening combination takes place in the centre of the beam at the inflexion point, while the two ends lie outside this zone. As a consequence, the beam in the matrix at the inflexion point develops an S-shape. Both the tail-shape of the middle beam and the S-shape of the beam at the inflexion point are also recognizable from the attitude of the finite strain ellipses (Fig. 3).

In Fig. 5a the incremental strain rate in a direction parallel to the layer interfaces is shown within the matrix. This layer-parallel direction has been calculated at every point within the matrix by constructing the shortest line between the two-layer interfaces bounding the matrix and taking the normal direction to this line. The layer-parallel strain rates have then been calculated from the numerically calculated strain rates by the usual coordinate transformation rules. Negative values (blue) indicate layer-parallel shortening while positive values (green to red) indicate layer-parallel extension. The boundary between these two regimes is indicated with a black line where layer-parallel strain rate is equal to zero. The area with positive values is referred to as area of incremental flattening. Fig. 5b shows the area (red) of the matrix in which finite flattening occurs. Finite flattening is here calculated based on the initial distance between the two layers. Finite flattening is active if the minimum distance between the two-layer interfaces is smaller than at the onset of the deformation. The evolution of the areas of incremental flattening (bounded by the zero-contour line for layer-parallel strain rates) and finite flattening are compared in Fig. 6a. The area of finite flattening is always smaller than the area of incremental flattening.

The smallest distance between the layer interfaces is situated near the inflexion point while the longest distance is in the hinge region. Continuous layer-parallel shortening in the hinge region leads to a steady increase of the distance between the layers (dots, Fig. 6b). In the region near the inflexion point (crosses) the distance between the layers first increases and then decreases. The maximum of the line marked by crosses indicates the transition from incremental matrix thickening to incremental matrix flattening. The point (around 30% bulk shortening in Fig. 6b) at which the line marked by crosses falls below the value 1 (i.e. the current distance equals the initial distance) indicates the onset of finite flattening.

4. Asymmetric parasitic folds in multilayer systems

A stack of thin multilayers is now placed between the two thick layers (Fig. 7). Table 2 lists the values of the used parameters. All thin layers have the same thickness and are 50 times

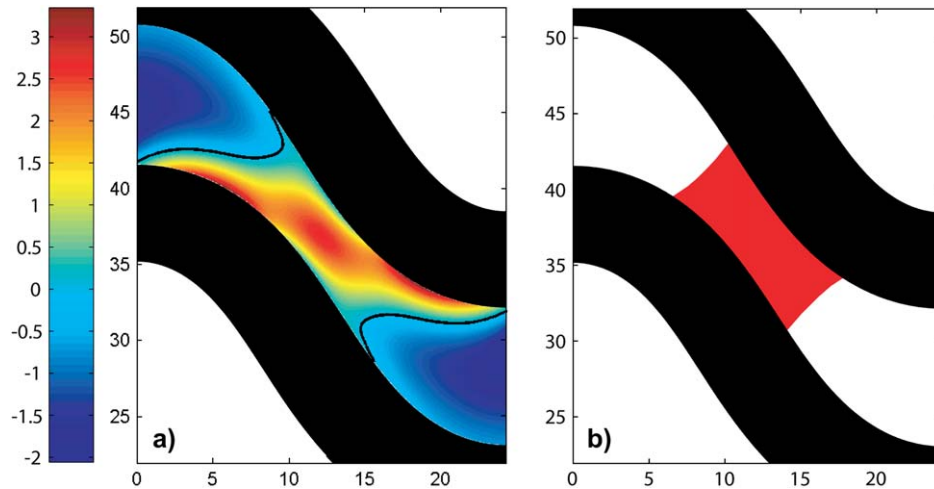


Fig. 5. (a) Incremental layer-parallel strain rate in the material between the two layers shown in Fig. 3. The black line represents the contour where the incremental strain rate is zero, and defines the transition between layer-parallel shortening (blue) and layer-parallel extension (red). The area between the two contour lines represents the area of incremental flattening in direction normal to the layer interfaces. (b) The red area defines the area of finite flattening, which is defined as the area, in which the distance between the two-layer interfaces is smaller than at the initial stage.

thinner than the thick layers to guarantee wavelengths of the parasitic folds at least one order of magnitude smaller than the first-order fold. The interlayers are three times the thickness of the thin layers. The viscosity of the thick and thin layers is the same, 100 times higher than the viscosity of the embedding material. Note that in Ramberg's (1963) experiments the thick layers were weaker than the thin layers to delay fold amplification of the thick layers relative to the thin layers. The focus in these experiments is on the deformation of the thin layers; the thick layers are used to generate folds larger than the parasitic folds that develop on the thin layers. To allow folding of thin layers before that of thick layers, the initial ratio of amplitude to layer thickness is set smaller for the thick layers than for the thin layers. Both thick layers initially have the same sinusoidal perturbation corresponding

to the dominant wavelength and the same initial ratio of amplitude to layer thickness. In contrast, all thin layers have a random perturbation (white noise) of the layer interface (see Mancktelow, 2001, for the impact of various initial geometrical irregularities on single-layer folding). Each layer interface of the thin layers had a different initial random perturbation to introduce as much geometrical randomness as possible.

Fig. 7 shows the deformed multilayer sequence with 15 thin layers after 50% bulk shortening. The initial ratio of amplitude to thickness (A/H) of the thick layers was 10^{-3} , 2×10^{-4} and 10^{-4} , and in the thin layers the average ratio of initial amplitude to layer thickness was always 0.1. For $A/H = 10^{-3}$ (Fig. 7a) there are parasitic folds in the hinge region only. Near the inflexion point, the thin layers are straight. Small parasitic folds are developed in the transition zone. Most parasitic

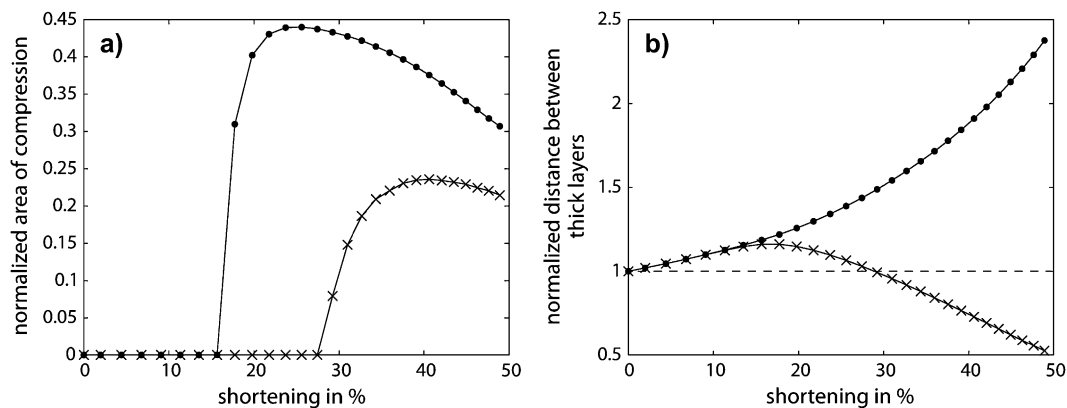


Fig. 6. (a) The line with dots shows the evolution of the area of incremental flattening divided by the whole area between the two layers (see also Fig. 5a). Until around 15% bulk shortening, there is no layer-parallel extension, only shortening. The line with crosses shows the evolution of the area of finite flattening divided by the whole area between the two layers (see also Fig. 5b). Finite flattening starts later than incremental flattening. Both areas of flattening exhibit a maximum. (b) The line with dots shows the evolution of the distance between the two layers in the hinge. The distance is divided by the initial distance between the two layers. This distance is continuously increasing. The line with crosses shows the evolution of the minimum distance between the two layers, which occurs between the inflexion points of the layers. The maximum indicates the transition from incremental shortening to incremental flattening. When the line decreases below the value of one, finite flattening starts.

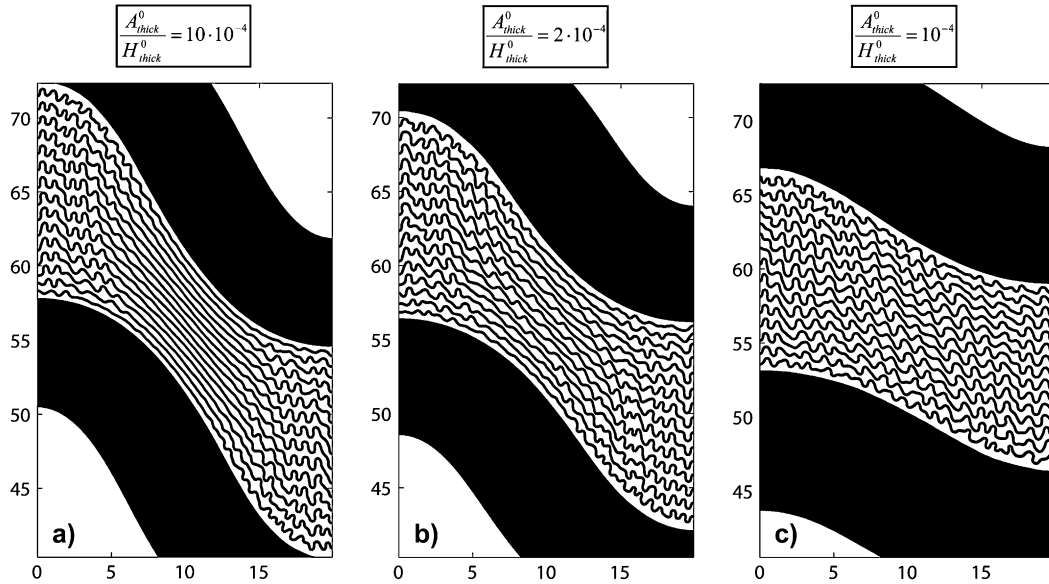


Fig. 7. Deformed multilayer sequence consisting of 15 thin layers placed between two thicker layers after 50% bulk shortening. Three different models are shown with a different initial ratio of amplitude to layer thickness for the thick layers. (a) 10×10^{-4} , (b) 2×10^{-4} and (c) 10^{-4} . The thick layers initially exhibited a sinusoidal perturbation, whereas each of the interfaces of the thin layers initially exhibited a random (white noise) perturbation with an average ratio of amplitude to thickness of 0.1.

for $A/H = 10^{-4}$ (Fig. 7c) the parasitic folds are strongly developed everywhere on the thin layers and are asymmetric in the limb region. The simulation with $A/H = 2 \times 10^{-4}$ (Fig. 7b) develops also parasitic folds

everywhere on the thin layers with a distinct asymmetry in the limb area. The ratio between the initial amplitudes of the thick and thin layers strongly controls the development of the parasitic folds, because the smaller the initial amplitude

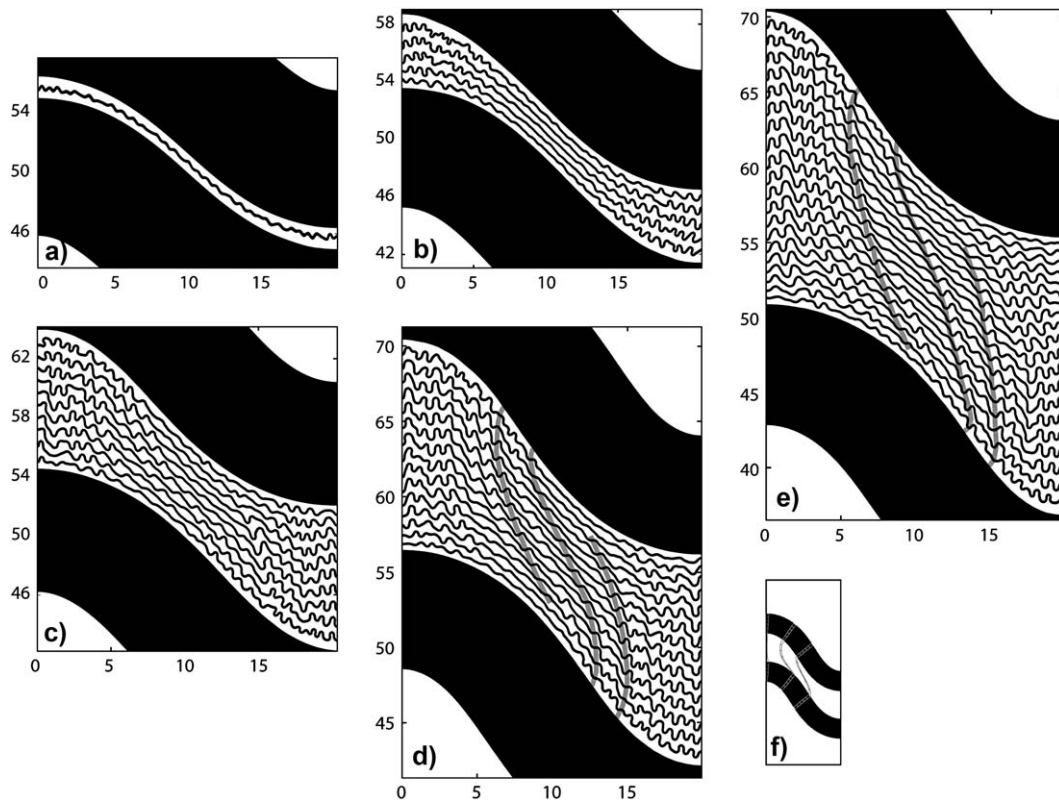


Fig. 8. (a)–(e) Geometry of five different multilayer models after 50% bulk shortening. The five models only differ in the number of thin layers (1, 5, 10, 15 and 20) between the two thick layers. (f) Internal geometry between the two layers of a double layer system after 50% bulk shortening (see also Fig. 4).

of the thick layers, the longer the parasitic folds can amplify in a pure shear environment. The more the amplitudes of the large fold grow, the stronger the simple shear and flattening deformation between the limbs, which hampers amplification of the parasitic folds.

The number of layers influences the amplification rates of multilayers (e.g., Ramberg, 1961; Schmid and Podlachikov, 2006) and Fig. 8 shows the results after 50% bulk shortening of five models with different numbers of thin layers. The ratio of initial amplitude to thickness of the thick layers was 2×10^{-4} (such as in Fig. 7b). The parasitic folds evolve differently for different numbers of thin layers. For one and five thin layers (Fig. 8a and b), the parasitic folds mainly develop in the hinge region of the large fold, where they are approximately symmetric. Between the limbs of the thick layers the thin layers are almost straight. The 10-layer-model (Fig. 8c) shows higher amplitude symmetric folds in the hinge region than in the one- and five-layer models. The amplitudes of the parasitic folds decrease from hinge to inflexion point of the larger fold. The parasitic folds near this inflexion point are asymmetric (S-shaped for the displayed part of the fold). Models with 15 and 20 thin layers (Fig. 8d and e) show even more distinct asymmetric parasitic fold shapes between the fold limbs of the two thick layers. They have very well developed S-shapes with

relatively high amplitude. As in the previous models, the amplitudes increase towards the hinge of the larger fold, where the parasitic folds are symmetric. Note that Fig. 8d is the same as Fig. 7b. The arrangement of the hinges of the parasitic folds, which initially were lying on top of each other during the pure shear deformation stage, is close to the shape of the deformed beams which described the strain in the matrix (Figs. 8d–f and 9a–9d, grey lines connect hinges of the parasitic folds initially lying on top of each other). The difference between these five models is the amplification of the thin layers. If the layer spacing is similar to the layer thickness, such as here, then the more layers a multilayer stack is made of (up to a certain saturation value), the faster the individual thin layers amplify (e.g., Ramberg, 1961; Schmid and Podlachikov, 2006). A model with more thin layers leads to higher amplitudes of the thin layers at the initiation of buckling of the thick layers.

Like in the two-layer model (Fig. 6b), the longest distance between the thick layers continuously increases (line with dots, Fig. 9e), and the evolution of the smallest distance with shortening shows a maximum (line with crosses, Fig. 9e). This maximum indicates the onset of flattening between the thick limbs, which decreases the amplitudes of the parasitic folds (Fig. 9c and d). The average value of all the

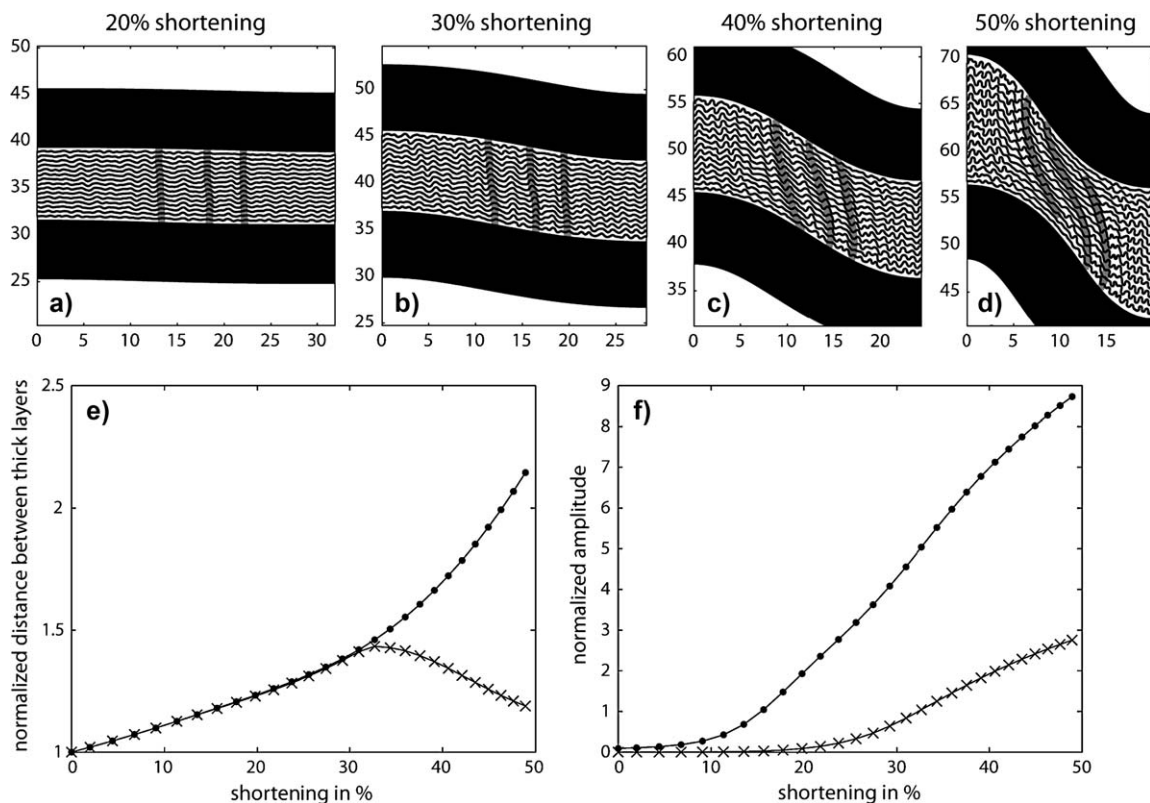


Fig. 9. (a)–(d) Four stages of deformation of a multilayer stack with 15 thin layers and two thick layers. (e) The line with dots shows the evolution of the distance between the two thick layers in the hinge. The distance is normalized by the initial distance between the thick layers. The line with crosses shows the evolution of the minimum distance between the two thick layers, which occurs between the inflexion points of the thick layers. This evolution of layer distances is very similar to the case without thin layers between the thick layers (Fig. 6). (f) The line with dots shows the evolution of the average amplitude of the thin layers in the hinge zone of the large scale fold. The amplitudes are normalized by the initial thickness of the thin layers. The line with crosses shows the average amplitude of the thick layers normalized by their initial thickness.

amplitudes of the thin layers in the hinge region of the larger fold (line with dots, Fig. 9f) increases continuously as well as the average amplitude of the thick layers (line with crosses, Fig. 9f).

The evolution of the distances between the two thick layers with and without thinner layers is very similar (Figs. 6b and 9e), suggesting that the fold amplification of the thick layers is only slightly modified by the folding of the thin layers. The same simulation as shown in Fig. 9 has been performed without thin layers, keeping the initial distance of the thick layers the same. The fold shape of the thick layers after 50% bulk shortening is nearly identical for the two simulations, confirming that folding of the thin layers has little effect on the larger folding (transparent grey shows the two folded thick layers without thinner layers, Fig. 10).

5. Discussion

The model setup used in this study is close to that used by Ramberg (1963) and is probably one of the simplest to generate parasitic folds. Clearly, other rheologies and model setups may produce comparable results, such as power-law rheology (Fletcher, 1974), viscoelasticity (Schmalholz and Podladchikov, 1999), anisotropy (Biot, 1965; Mühlhaus et al., 2002) or slip between layers (Pfaff and Johnson, 1989). However, despite more complex scenarios, it can be expected that the fundamental evolution of asymmetric parasitic folds remains the same, namely that symmetric buckle-folds are first generated and

then sheared into an asymmetric form by the development of a larger structure.

We used differences in the ratio of initial amplitude to layer thickness to delay the amplification of the thick layers relative to the thin layers. In nature, layers composed of different rock types are never perfectly flat and undulations with characteristic amplitudes exist due to, for example, sedimentary structures (e.g., wave ripples) or metamorphic processes (e.g., crenulation). The absolute values of the amplitudes of these undulations can be expected to be often independent of the thickness of the layers that bear them. For example, the amplitudes of wave ripples will be more or less the same on sandstone layers of 10 cm or 1 m thickness. Therefore, the ratio of amplitude to layer thickness can be expected to be relatively larger in thin layers than in thick layers, such as assumed in our study.

Several numerical simulations with a bell-shaped (Biot et al., 1961) instead of a sinusoidal perturbation on the interfaces of the thick layers (Fig. 11) and simulations with viscosity contrasts of 40 and 50 have been performed in addition to test the robustness of our numerical results. All additional numerical simulations confirm the fundamental results for parasitic folding presented in this study.

6. Conclusions

- (1) Our numerical simulations verified Ramberg's (1963) theory of parasitic fold development for Newtonian viscous materials. Asymmetric, S- and Z-shaped parasitic folds

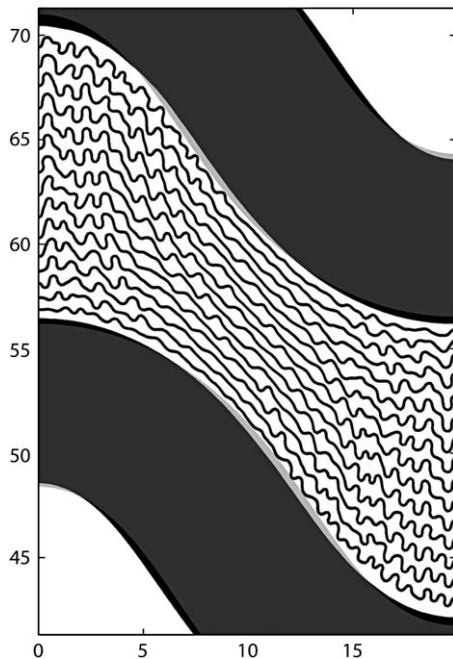


Fig. 10. The black layers show the folded multilayer system with 15 thin layers after 50% bulk shortening. The two transparent grey layers (also 50% bulk shortening) exhibited the same initial conditions than the thick black layers, but without thin layers in between. The comparison between the thick black and thick grey layers indicates that the fold evolution of the thick black layers is only slightly modified by the presence of the thin layers.

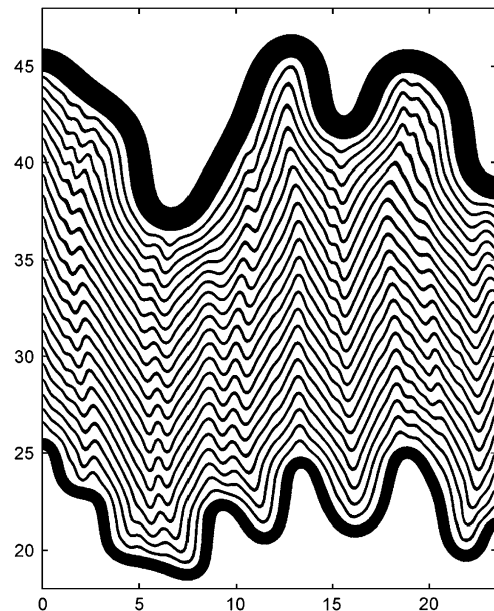


Fig. 11. Numerical simulation of parasitic folding for more complex geometries and 22 thin layers. The two external layers have different thicknesses and initially had a bell-shaped perturbation of the layer interface. The thin layers had initially a random perturbation. In all layers a true wavelength selection took place. The folds in the external layers have different wavelengths due to their different thickness. The simulation shows both S- and Z-shaped asymmetric, and M-shaped symmetric parasitic folds.

originate from symmetric buckle-folds that are sheared into an asymmetric shape by the relative displacement between the thick layers that control the larger folds in which parasitic folds occur.

- (2) The timing between the amplification of the parasitic folds and the amplification of the larger fold controls the development of asymmetric folds in the limb zone of the larger fold. If the larger fold amplifies while the parasitic folds still have small amplitudes, no asymmetric parasitic folds develop because early buckles are unfolded by the flattening between the thick layers in the limbs of the larger fold.
- (3) In contrast, the parasitic folds in the hinge zone of the larger fold remain symmetric (M-shaped) because the deformation there is dominantly pure shear. These symmetric, M-shaped parasitic folds always develop independently of the relative timing between their amplification and that of the larger folds.
- (4) A larger number of thin layers between two thick layers favour the development of distinct asymmetric parasitic folds, because a large number of thin layers has a larger amplification rate and requires less shortening to develop high amplitude parasitic folds than few layers.

Acknowledgements

This work resulted from a master thesis of Marcel Frehner at the Structural Geology and Tectonics Group of ETH Zurich. Helpful comments on the manuscript and technical support of Jean-Pierre Burg are gratefully acknowledged. We thank Bruce Hobbs for a detailed and constructive review. A second anonymous review is acknowledged. We further thank Guy Simpson, Neil Mancktelow and Dani Schmid for helpful comments and stimulating discussions.

Appendix

This appendix summarizes the self-developed finite element algorithm which was used in this study. The conservation equations for slow incompressible flow in the absence of body forces in two dimensions are (e.g., Bathe, 1996; Haupt, 2002):

$$\begin{aligned} \frac{\partial \sigma_{xx}}{\partial x} + \frac{\partial \sigma_{xy}}{\partial y} &= 0 \\ \frac{\partial \sigma_{xy}}{\partial x} + \frac{\partial \sigma_{yy}}{\partial y} &= 0 \end{aligned} \tag{A1}$$

$$\frac{\partial p}{\partial t} = -K \left(\frac{\partial v_x}{\partial x} + \frac{\partial v_y}{\partial y} \right) \tag{A2}$$

where σ_{xx} and σ_{yy} are components of the total stress tensor in the x - and y -direction, respectively, σ_{xy} is the shear stress, p is the pressure, K is the compressibility parameter and v_x and v_y are the velocities in x - and y -direction. Eq. (A1) represents conservation of linear momentum and Eq. (A2) represents conservation of mass. Eq. (A2) deviates from the standard

form for incompressible flow (i.e. $(\partial v_x/\partial x) + (\partial v_y/\partial y) = 0$), but is only applied for very large values of K , so that the resulting divergence of the velocity field goes to zero, which means to 10^{-15} in this study. Application of Eq. (A2) is often referred to as the penalty approach for incompressible flow (e.g., Cuvelier et al., 1986; Hughes, 1987). The constitutive equations for a linear viscous rheology are:

$$\begin{aligned} \begin{Bmatrix} \sigma_{xx} \\ \sigma_{yy} \\ \sigma_{xy} \end{Bmatrix} &= -p \begin{Bmatrix} 1 \\ 1 \\ 0 \end{Bmatrix} \\ &+ \underbrace{\frac{1}{3}\mu \begin{bmatrix} 4 & -2 & 0 \\ -2 & 4 & 0 \\ 0 & 0 & 3 \end{bmatrix}}_{\mathbf{D}} \begin{Bmatrix} \partial v_x/\partial x \\ \partial v_y/\partial y \\ \partial v_x/\partial y + \partial v_y/\partial x \end{Bmatrix} \end{aligned} \tag{A3}$$

with μ the Newtonian viscosity. Discretization of the governing equations and numerical integration is performed using the isoparametric Q9/3-element with nine nodes for the biquadratic continuous velocity degrees of freedom and three for the linear discontinuous pressure degrees of freedom (Fig. A1, e.g., Hughes, 1987). After discretization the governing equations are given as (e.g., Hughes, 1987):

$$\begin{bmatrix} \mathbf{K} & \mathbf{Q} \\ \mathbf{Q}^T & -\frac{\mathbf{M}}{K \Delta t} \end{bmatrix} \begin{Bmatrix} \tilde{\mathbf{v}} \\ \tilde{p}^{new} \end{Bmatrix} = \begin{Bmatrix} 0 \\ -\frac{\mathbf{M}}{K \Delta t} \tilde{p}^{old} \end{Bmatrix} \tag{A4}$$

where swung dashes denote vectors containing nodal values of the respective variables. The time derivative in Eq. (A2) has been replaced by a finite difference quotient with Δt being

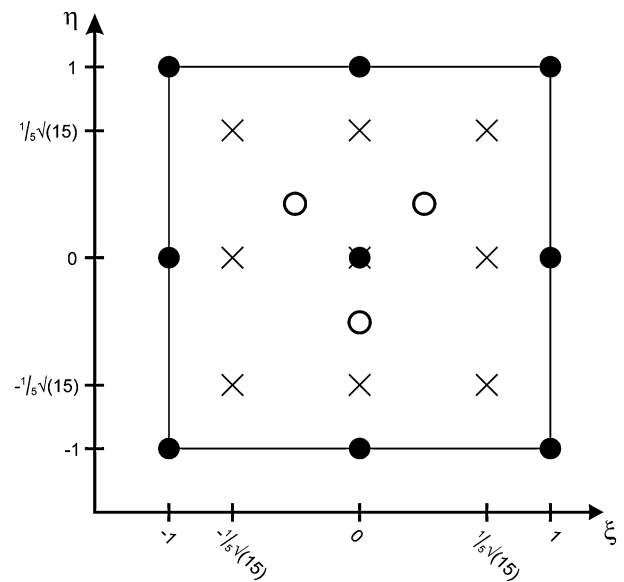


Fig. A1. Local reference element used for the numerical solution, with nine nodes for velocity degrees of freedom (filled circles), three for the pressure degrees of freedom (circles) and nine integration points (crosses). ξ and η are the local coordinates.

the time increment ($\partial p / \partial t \approx (p^{\text{new}} - p^{\text{old}}) / \Delta t$). The three matrices \mathbf{K} , \mathbf{Q} and \mathbf{M} are:

$$\begin{aligned} \mathbf{K} &= \iint \mathbf{B}^T \mathbf{D} \mathbf{B} \, dx \, dy, \quad \mathbf{Q} = - \iint \mathbf{B}_G^T \mathbf{N}_P \, dx \, dy, \\ \mathbf{M} &= \iint \mathbf{N}_P^T \mathbf{N}_P \, dx \, dy \end{aligned} \quad (\text{A5})$$

where vector \mathbf{N}_P contains the pressure shape functions and matrix \mathbf{B} and vector \mathbf{B}_G contain spatial derivatives of the velocity shape functions in a suitable organized way (e.g., Zienkiewicz and Taylor, 1994). The integrations are performed numerically using nine integration points per element (Fig. A1). Using discontinuous pressure shape functions allows the elimination of the pressure at the element level. This elimination leads to a system involving only unknown velocities:

$$\mathbf{L} \tilde{\mathbf{v}} = -\mathbf{Q} \tilde{\mathbf{p}}^{\text{old}} \quad (\text{A6})$$

where

$$\mathbf{L} = \mathbf{K} + K \Delta t \mathbf{Q} \mathbf{M}^{-1} \mathbf{Q}^T \quad (\text{A7})$$

Values of $\tilde{\mathbf{p}}^{\text{new}}$ are restored during the Uzawa-type iteration algorithm, during which Eq. (A6) is solved iteratively with updated values of $\tilde{\mathbf{p}}^{\text{old}}$ until the divergence of the velocity converges towards zero (i.e. 10^{-15} , e.g., Pelletier et al., 1989). After every time step, the resulting velocities are used to move the nodes of each element with the displacements resulting from the product of velocities times time step (i.e. explicit time integration). Then, the new velocities are again calculated for the new grid.

The developed finite element algorithm has been successfully tested twice. First, by correctly reproducing the analytical growth rate (Fletcher, 1977) for single-layer folding, and second, by correctly reproducing the analytical pressure field around a rigid inclusion (Schmid and Podladchikov, 2003).

References

- Bathe, K.-J., 1996. Finite Element Procedures. Prentice Hall, Upper Saddle River, New Jersey.
- Biot, M.A., 1961. Theory of folding of stratified viscoelastic media and its implications in tectonics and orogenesis. *Geological Society of America, Bulletin* 72, 1595–1620.
- Biot, M.A., 1965. Mechanics of Incremental Deformations. John Wiley & Sons, Inc., New York.
- Biot, M.A., Ode, H., Roever, W.L., 1961. Experimental verification of the theory of folding of stratified viscoelastic media. *Geological Society of America, Bulletin* 72 (Nov.), 1621–1632.
- Casey, M., Huggenberger, P., 1985. Numerical modelling of finite-amplitude similar folds developing under general deformation histories. *Journal of Structural Geology* 7 (1), 103–114.
- Cobbold, P.R., Cosgrove, J.W., Summers, J.M., 1971. Development of internal structures in deformed anisotropic rocks. *Tectonophysics* 12, 23–53.
- Cuvelier, C., Segal, A., van Steenhoven, A.A., 1986. Finite Element Methods and the Navier–Stokes Equations. D. Reidel Publishing Company.
- Debremaecker, J.C., Becker, E.B., 1978. Finite element models of folding. *Tectonophysics* 50, 349–367.
- DeSitter, L.U., 1964. Structural Geology. McGraw-Hill Book Company, New York.
- Fletcher, R.C., 1974. Wavelength selection in the folding of a single-layer with power-law rheology. *American Journal of Science* 274 (11), 1029–1043.
- Fletcher, R.C., 1977. Folding of a single viscous layer: exact infinitesimal-amplitude solution. *Tectonophysics* 39, 593–606.
- Ghosh, S.K., 1968. Experiments of buckling of multilayers which permit inter-layer gliding. *Tectonophysics* 6 (3), 207–249.
- Haupt, P., 2002. Continuum Mechanics and Theory of Materials. Springer, Berlin.
- Hughes, T., 1987. The Finite Element Method. Dover Publications, Mineola, New York.
- Johnson, A.M., 1969. Development of folds within Carmel Formation, Arches national monument, Utah. *Tectonophysics* 8 (1), 31–77.
- Johnson, A.M., Fletcher, R.C., 1994. Folding of Viscous Layers. Columbia University Press, New York.
- Mancktelow, N.S., 2001. Single layer folds developed from initial random perturbations: the effects of probability distribution, fractal dimension, phase and amplitude. In: Koyi, H.A., Mancktelow, N.S. (Eds.), *Tectonic Modeling: A Volume in Honor of Hans Ramberg*. Geological Society of America, Boulder, pp. 69–87. *Memoir* 193.
- Mühlhaus, H.B., Moresi, L., Hobbs, B., Dufour, F., 2002. Large amplitude folding in finely layered viscoelastic rock structures. *Pure Applied Geophysics* 159, 2311–2333.
- Pelletier, D., Fortin, A., Camarero, R., 1989. Are FEM solutions of incompressible flows really incompressible? (Or how simple flows can cause headaches). *International Journal for Numerical Methods in Fluids* 9, 99–112.
- Pfaff, V.J., Johnson, A.M., 1989. Opposite sense of fold asymmetry. *Engineering Geology* 27, 3–38.
- Ramberg, H., 1961. Contact strain and folding instability of a multilayered body under compression. *Geologische Rundschau* 51, 405–439.
- Ramberg, H., 1963. Evolution of drag folds. *Geological Magazine* 100 (2), 97–110.
- Ramberg, H., 1964. Selective buckling of composite layers with contrasted rheological properties, a theory for simultaneous formation of several orders of folds. *Tectonophysics* 1 (4), 307–341.
- Ramberg, H., Strömgaard, K.-E., 1971. Experimental tests of modern buckling theory applied on multilayered media. *Tectonophysics* 11, 461–472.
- Ramsay, J.G., Huber, M.I., 1983. Strain Analysis. In: *The Techniques of Modern Structural Geology*, vol. 1. Academic Press, London.
- Ramsay, J.G., Huber, M.I., 1987. Folds and Fractures. In: *The Techniques of Modern Structural Geology*, vol. 2. Academic Press, London.
- Schmalholz, S.M., Podladchikov, Y., 1999. Buckling versus folding: importance of viscoelasticity. *Geophysical Research Letters* 26 (17), 2641–2644.
- Schmalholz, S.M., Podladchikov, Y.Y., Schmid, D.W., 2001. A spectral/finite difference method for simulating large deformations of heterogeneous, viscoelastic materials. *Geophysical Journal International* 145 (1), 199–208.
- Schmid, D.W., Podladchikov, Y.Y., 2006. Fold amplification rates and dominant wavelength selection in multilayer stacks. *Philosophical Magazine* 86 (21–22), 3409–3423.
- Schmid, D.W., Podladchikov, Y.Y., 2003. Analytical solutions for deformable elliptical inclusions in general shear. *Geophysical Journal International* 155, 269–288.
- Thomasset, F., 1981. Implementation of Finite Element Methods for Navier–Stokes Equations. Springer-Verlag, New York.
- Williams, E., 1961. The deformation of confined, incompetent layers in folding. *Geological Magazine* 98 (4), 317–323.
- Zienkiewicz, O.C., Taylor, R.L., 1994. The Finite Element Method. McGraw-Hill Book Company, London.